Characterizing Earth gravity field fluctuations with the MIGA antenna for future gravitational wave detectors

J. Junca,[1] A. Bertoldi,[1] D. O. Sabulsky,[1] G. Lefèvre,[1] X. Zou,[1] J.-B. Decitre,[2] R. Geiger,[3]
A. Landragin,[3] S. Gaffet,[2] P. Bouyer,[1] and B. Canuel[1]

[1]*LP2N, Laboratoire Photonique, Numérique et Nanosciences,*
Université Bordeaux-IOGS-CNRS:UMR 5298, rue F. Mitterrand,
F-33400 Talence, France
[2]*LSBB, Laboratoire Souterrain Bas Bruit, UNS, UAPV, CNRS:UMS 3538, AMU,*
La Grande Combe, F-84400 Rustrel, France
[3]*LNE-SYRTE, Observatoire de Paris, Université PSL, CNRS, Sorbonne Université,*
61, avenue de l'Observatoire, F-75014 Paris, France

Fluctuations of the Earth's gravitational field are a major noise source for ground-based experiments investigating general-relativistic phenomena such as gravitational waves (GWs). Mass density variations caused by local seismic or atmospheric perturbations determine spurious differential displacements of the free-falling test masses—called gravity gradient noise (GGN)—which mimics GW effects. This GGN is expected to become dominant in the infrasound domain and must be tackled for the future realization of observatories exploring GWs at low frequency. GGN will be studied with the MIGA experiment, a demonstrator for low-frequency GW detection based on atom interferometry currently being constructed at the low-noise underground Laboratoire Souterrain à Bas Bruit (LSBB) in France. MIGA will provide precise measurements of local gravity, probed by a network of three free-falling atom test masses separated by up to 150 m. We model the effect of GGN for MIGA and use seismic and atmospheric data recorded at LSBB to characterize their impact on future measurements. We show that the antenna will be able to characterize GGN using dedicated data analysis methods.

I. INTRODUCTION

The first detection of gravitational waves (GWs) [1] by the LIGO interferometer [2] unveiled a new vantage point to study the Universe through the observation of phenomena hidden to electromagnetic detectors such as merging black holes [3], and later gave rise to multimessenger astronomy when the localization of a binary neutron star inspiral by the LIGO [2] and VIRGO [4] association lead to the combined electromagnetic and gravitational observation of the event [5,6]. These novel possibilities define the field of GW astronomy. Whereas existing GW detectors will keep observing events in their sensitivity window (from a few tens of Hz to 1 kHz [7]), important scientific arguments propose extending the detection bandwidth to lower frequency regimes; a wealth of sources are expected in the infrasound band [8] (from 10 mHz to 1 Hz) and tracking signals at these frequencies will improve the parameter estimation for events later entering the detection bandwidth of current GW detectors or enable their precise localization in the sky for optical observations [9,10]. The main problem with extending the sensitivity bandwidth of present GW detectors at low frequency is posed by seismic noise [7] and gravity gradient noise (GGN). This effect,

also called Newtonian noise, is produced by density variations within the medium surrounding the detector and causes spurious differential displacements of the free-falling test masses [11,12].

One solution is to develop space-based detectors to exploit high-quality geodetic motion provided by drag-free satellites; this is the case of the laser interferometers eLISA [13] and DECIGO [14], as well as several proposals relying on ultracold atomic sensors [15], in the form of both atom interferometers (AIs) [16,17] and atomic clocks [18]. Other approaches rely on improved technologies on Earth [19] to reduce the impact of low-frequency noise sources by improving the mechanical decoupling of the test masses from the environment via enhanced suspensions [19] or by opting for freely falling probes, which are possible using AIs [20]. Such solutions mitigate the problems created by seismic noise, but do not alter the effect of GGN.

It has been shown [21] that the impact of GGN can be strongly reduced by averaging the signals of several distant atom-interferometric gradiometers. Such configurations, which require precise GGN models, will be tested with the MIGA experiment [22], a demonstrator for low-frequency GW detection based on atom interferometry

currently being constructed at the low-noise underground Laboratoire Souterrain à Bas Bruit (LSBB) in France. MIGA will provide precise measurements of the local gravity on a baseline up to 150 m using a network of atom gradiometers. In this article, we model the effect of GGN on MIGA and study possible measurement protocols to validate such models with future data from the antenna.

The article is organized as follows. Section II introduces the sensitivity to GW for a gradiometer based on atom interferometry. We then present projections of the equivalent strain induced by local gravitational field fluctuations using seismic (Sec. III) and atmospheric (Sec. IV) data measured at the site where MIGA is being built. In Sec. V we then show that MIGA could observe cumulative effects induced by GGN and test the validity of the models used in this article.

II. GGN AND GRAVITY-GRADIOMETRY BASED ON AI

A. Strain limitations from GGN

In this section, we consider a single gradiometer using two free-falling atom test masses and calculate the strain sensitivity limitation induced by the differential acceleration of the test masses. We consider two correlated AIs placed at positions $X_{i,j}$ along the x axis, created by Bragg diffraction on the standing wave obtained by the retroreflection of an interrogating laser (Fig. 1). A three-pulse sequence ($\pi/2$-π-$\pi/2$) applied to the two atomic ensembles along the x direction produces the interferometric signal, which is read out as a population unbalance, and depends on the phase difference $\Delta\varphi_{\text{las}}$ between the two counterpropagating beams. Considering a large momentum transfer diffraction, i.e., $2n$ photons coherently exchanged during the diffraction process, the output atomic phase $\Delta\phi_x(X_i, t)$ of the interferometer at position X_i and time t is

$$\Delta\phi_x(X_i, t) = n\int_{-\infty}^{\infty} \Delta\varphi_{\text{las}}(X_i, \tau)g'(\tau - t)d\tau + \epsilon(X_i, t),$$

$$(1)$$

where g' is the time derivative of the sensitivity function of the three-pulse AI [23] and $\epsilon(X_i, t)$ is the detection
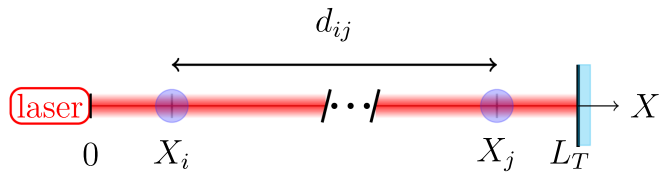

FIG. 1. Gravity gradiometer realized with two AIs placed at $X_{i,j}$, separated by a distance d_{ij}, and coherently manipulated by a common laser retroreflected by a mirror placed at position L_T. The specific configuration of the MIGA antenna will use a distance of 150 m, an interrogation wavelength of 780 nm linked to the use ^{87}Rb atoms, and a cycling time of 2 Hz.

noise related to the projection of the atomic wave function during the measurement process. Taking into account the effects of laser frequency noise $\delta\nu(\tau)$, the vibration of the retroreflecting mirror $\delta x_{\text{mir}}(\tau)$, the GW strain variation $h(\tau)$, and the fluctuation of the mean trajectory of the atoms along the laser beam direction induced by the fluctuating local gravitational field $\delta x_{at}(X_i, \tau)$, the last equation can be written as [21]

$$\Delta\phi_x(X_i, t) = \int_{-\infty}^{\infty} 2nk_L\left[\left(\frac{\delta\nu(\tau)}{\nu} + \frac{h(\tau)}{2}\right)(L_T - X_i)\right.$$
$$\left. + \delta x_{\text{mir}}(\tau) - \delta x_{at}(X_i, \tau)\right]g'(\tau - t)d\tau$$
$$+ \epsilon(X_i, t), \qquad (2)$$

where $k_L = \frac{2\pi\nu}{c}$ is the wave number of the interrogation laser. By simultaneously interrogating two AIs with the same laser (Fig. 1), one can cancel, to first order, the motion of the retroreflecting mirror. The resulting differential phase $\psi(X_i, X_j, t)$ is

$$\psi(X_i, X_j, t) = \Delta\phi_x(X_i, t) - \Delta\phi_x(X_j, t)$$
$$= \int_{-\infty}^{\infty} 2nk_L\left[\left(\frac{\delta\nu(\tau)}{\nu} + \frac{h(\tau)}{2}\right)d_{ij}\right.$$
$$\left. + \delta x_{at}(X_j, \tau) - \delta x_{at}(X_i, \tau)\right]g'(\tau - t)d\tau$$
$$+ \epsilon(X_i, t) - \epsilon(X_j, t). \qquad (3)$$

For the sake of clarity we will now neglect the laser frequency noise $\delta\nu(t)$: for MIGA this contribution is expected to be well below the initial sensitivity of the detector [22]. Further, for higher sensitivity configurations, a detector geometry with two orthogonal arms can be used to cancel out the effects of laser frequency noise while preserving sensitivity to $(+)$ polarized GWs. We can write the power spectral density (PSD) of the differential interferometric phase as

$$S_\psi(d_{ij}, \omega) = (2nk_L)^2\left[d_{ij}^2\frac{S_h(\omega)}{4} + S_{\Delta x}(d_{ij}, \omega)\right]|\omega G(\omega)|^2$$
$$+ 2S_\epsilon(\omega), \qquad (4)$$

given that the detection noise is spatially uncorrelated. The term $G(\omega)$ represents the Fourier transform of the sensitivity function of the interferometer to phase variations [23],

$$|\omega G(\omega)| = 4\sin^2\left(\frac{\omega T}{2}\right), \qquad (5)$$

where T is the time interval between two successive pulses of the interferometer.

In Eq. (4) the term $S_{\Delta x}(d_{ij}, \omega)$ is the PSD of the differential displacement of the atom test masses with respect to the interrogation laser,

$$S_{\Delta x}(d_{ij},\omega) = \frac{S_{\Delta a_x}(d_{ij},\omega)}{\omega^4}, \qquad (6)$$

where $S_{\Delta a_x}(d_{ij},\omega)$ is the PSD of the difference of the local gravitational field between the points X_i and X_j projected along the gradiometer direction, i.e., the GGN. This perturbation introduces an atomic phase variation that is indistinguishable from the signal produced by a GW, shown in Eq. (4), and constitutes a limit for the detector that sums up with detection noise.

To quantify and compare the possibility to detect GWs over various noise sources, taking the GW signal as the signal of interest in Eq. (4) and dividing it by the other terms, we obtain the signal-to-noise ratio (SNR) of the detector. Setting the limit of detectability for an SNR of 1, we define the strain sensitivity of the gradiometer as the sum

$$S_h(\omega) = \frac{4S_{\Delta a_x}(d_{ij},\omega)}{\omega^4 d_{ij}^2} + \frac{S_\epsilon(\omega)}{2(2nk)^2 d_{ij}^2 \sin^4(\frac{\omega T}{2})}. \qquad (7)$$

B. Spatial correlation of GGN

GGN originates from a series of different mechanisms [11], which are associated with different spatial correlation properties. We express GGN as a function of the correlation of the gravitational field variations δa_x between points X_i and X_j as

$$\begin{aligned} S_{\Delta a_x}(d_{ij},\omega) &= S\{\delta a_x(X_j) - \delta a_x(X_i)\}(\omega) \\ &= F\{[\delta a_x(X_j) - \delta a_x(X_i)] \\ &\quad \otimes [\delta a_x^*(X_j) - \delta a_x^*(X_i)]\}(\omega), \qquad (8) \end{aligned}$$

where $S\{.\}$, $F\{.\}$, and $\otimes$ denote the PSD, Fourier transform, and convolution operators, respectively. The last equation can be written as

$$S_{\Delta a_x}(d_{ij},\omega) = 2C(0,\omega) - C(d_{ij},\omega) - C(-d_{ij},\omega), \qquad (9)$$

where $C(d_{ij},\omega)$ is the Fourier transform of the two-point spatial correlation function of the gravitational field,

$$\begin{aligned} C(d_{ij},\omega) &= F\{\delta a_x(X_j) \otimes \delta a_x^*(X_i)\}(\omega) \\ &= F\{\delta a_x(X_j)\}(\omega) \times F\{\delta a_x^*(X_i)\}(\omega). \qquad (10) \end{aligned}$$

In the following, we will focus on the two contributions previously identified as the main limiting effects for GW detectors linked to density variations in the surrounding medium resulting from seismic activity [24,25] (Sec. III) and perturbations of the atmospheric pressure [24,26] (Sec. IV). For both contributions, we will calculate the different gravity correlation functions and project the impact of the associated GGN in terms of the strain

sensitivity using Eq. (7). This study is carried out for the configuration of the MIGA gravity antenna [22], which will generate gradiometric measurements from a network of three AIs regularly spaced on a baseline of 150 m.

III. SEISMIC GGN

The MIGA experiment is now under construction in southern France at the LSBB, an underground facility located away from major human activity and characterized by very low seismic noise. The seismic conditions within the laboratory are continuously monitored using a network of six broadband STS2 seismometers [27]. Figure 2 shows typical seismic spectra along the vertical axis, recorded by the station located at the center of the infrastructure ("RAS" station; see Ref. [27]). The data are compared to Peterson's model [28], which is usually taken as a reference to assess the seismic properties of a given site.
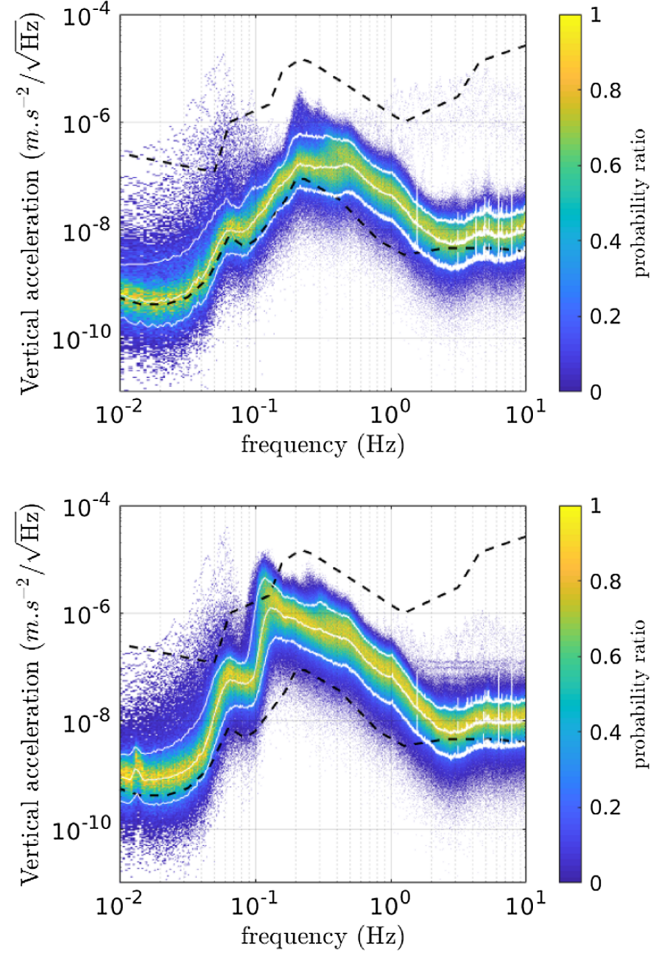

FIG. 2. Vertical acceleration spectra at LSBB compared to the high- and low-noise Peterson models [28], with the 10th, 50th, and 90th percentiles of the histogram represented by white lines. Top: The spectrum recorded during a quiet month (August 2011). Bottom: The spectrum recorded during a noisy month (February 2011).
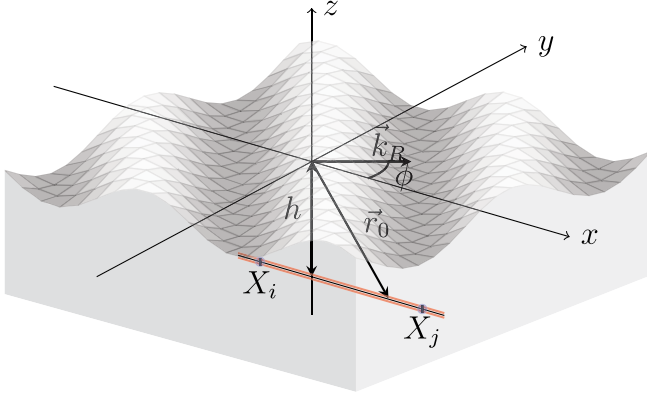
FIG. 3. Rayleigh wave modeling: angle and axis definition. $\vec{k}_R$ is the wave vector of the incident Rayleigh wave, ϕ is the azimuthal angle of the wave, h is the depth of the detector, $\vec{r}_0$ is the position where the gravity perturbation is calculated, and X_i and X_j are the positions of the extremities of the gradiometer along the X axis.

During quiet periods the seismic background activity at LSBB is close to the low Peterson model half of the time. During noisier periods, typically during winter, the seismic background noise is increased with a frequency signature that depends on sea and ocean conditions. In the infrasound band, the sea and ocean motion accounts for most of the microseismic activity that generates the continuous vertical oscillations of the Earth [29] that propagate as surface seismic waves (Love and Rayleigh waves). Love waves are pure shear waves that do not produce density variations [30] and thus do not produce GGN in an isotropic and homogeneous medium. Therefore, we confine our study to the case of Rayleigh waves and consider the total seismic field as an incoherent sum of monochromatic Rayleigh waves propagating isotropically in an isotropic and homogeneous medium over the different angular directions ϕ in the horizontal plane (see Fig. 3).

At an underground depth $h > 0$, the gravity potential perturbation $\delta U(\vec{r}_0, t)$ induced by Rayleigh waves propagating in the angular directions ϕ is [11]

$$\delta U(\vec{r}_0, t) = 2\pi G\rho_0 \frac{\xi_z(\omega)}{q_z^P - k_R\sqrt{q_z^P/q_z^S}} e^{i(\vec{k}_R \cdot \vec{r}_0 - \omega t)}$$
$$\times \left(-2e^{-hq_z^P} + \left(1 + \sqrt{q_z^P/q_z^S}\right) e^{-hk_R} \right), \quad (11)$$

where $\vec{k}_R$ is the wave vector, $\xi_z(\omega)$ is the vertical seismic displacement amplitude, ρ_0 is the average medium density, and G is the gravitational constant. Note that k_P and k_S are the wave vectors of the compressional (P-wave) and shear (S-wave) waves, where we have $q_z^P = \sqrt{k_R^2 - k_P^2}$ and $q_z^S = \sqrt{k_R^2 - k_S^2}$.

Assuming a linear dispersion with P-wave speed α, S-wave speed β, and Rayleigh wave speed c_R, the gravity

perturbation of Eq. (11) determines the longitudinal acceleration on a test mass at $\vec{r}_0$ as

$$\delta a_x(\vec{r}_0, t) = -\vec{\nabla}\delta U(\vec{r}_0, t).\vec{e}_x$$
$$= 2\pi G\rho_0\gamma\xi_z(\omega)e^{i(\vec{k}_R \cdot \vec{r}_0 - \omega t)}$$
$$\times [e^{-hk_R} + b(e^{-hq_z^P} - e^{-hk_R})]i\cos\phi, \quad (12)$$

where γ and b are dimensionless factors depending on the wave velocity ratios c_R/α and c_R/β, which themselves depend upon the mechanical properties of the propagating medium:

$$\gamma = \frac{\left(\frac{1-c_R^2/\alpha^2}{1-c_R^2/\beta^2}\right)^{\frac{1}{4}} - 1}{\left(\frac{1-c_R^2/\alpha^2}{1-c_R^2/\beta^2}\right)^{\frac{1}{4}} - \sqrt{1 - c_R^2/\alpha^2}}, \quad (13)$$

$$b = \frac{2}{1 - \left(\frac{1-c_R^2/\alpha^2}{1-c_R^2/\beta^2}\right)^{\frac{1}{4}}}. \quad (14)$$

For a test mass placed at $\vec{r}_0 = X\vec{e}_x - h\vec{e}_z$, Eq. (12) can be written as

$$\delta a_x(X, t) = \kappa_R(k_R)\xi_z(\omega)e^{-i\omega t}e^{ik_R X\cos\phi}i\cos\phi, \quad (15)$$

with

$$\kappa_R(k_R) := 2\pi G\rho_0\gamma[e^{-hk_R} + b(e^{-hq_z^P} - e^{-hk_R})]. \quad (16)$$

The spatial correlation of the seismic GGN for an underground gradiometer of baseline $d_{ij} = X_j - X_i$ can then be obtained from Eq. (10), averaging over all different directions ϕ,

$$C^R(d_{ij}, \omega) = \kappa_R^2(k_R)S_{\xi_z}(\omega)\langle\cos^2\phi \, e^{ik_R d_{ij}\cos\phi}\rangle_\phi$$
$$= \frac{1}{2}\kappa_R^2(k_R)S_{\xi_z}(\omega)[J_0(k_R d_{ij}) - J_2(k_R d_{ij})],$$
$$(17)$$

with J_n is the nth Bessel function of the first kind. Using Eq. (9) we obtain the associated GGN,

$$S_{\Delta a_x}(d_{ij}, \omega) = \kappa_R^2(k_R)S_{\xi_z}(\omega)\chi_1^R(k_R, d_{ij}), \quad (18)$$

where $\chi_1^R(k_R, d_{ij})$ gathers all correlation effects contributing to the GGN:

$$\chi_1^R(k_R, d_{ij}) = 1 - J_0(k_R d_{ij}) + J_2(k_R d_{ij}). \quad (19)$$

For short distances or low frequencies ($k_R d_{ij} \ll 1$), Eq. (19) is approximately
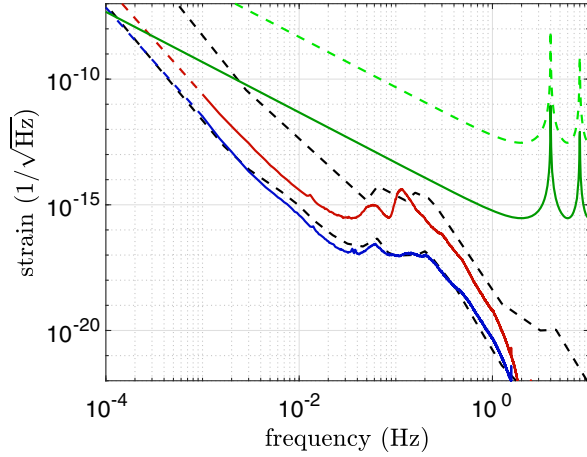
FIG. 4. The seismic GGN projection at LSBB is shown for the 10th percentile during a quiet month (blue curve) and the 90th percentile during a noisy month (red curve). The low-frequency behaviors of the two curves (shown as dashed lines) are extrapolated with a slope of −3.3 in accordance with the high- and low-noise Peterson models plotted with dashed black lines for comparison. The detection noises for MIGA in its initial and improved configurations, calculated for $2T = 0.5$ s, are shown as dashed and plain green lines, respectively.

$$\chi_1^R(k_R, d_{ij}) \simeq \frac{3}{8} k_R^2 d_{ij}^2. \tag{20}$$

Taken with Eq. (7), this means that the strain sensitivity limitations from GGN are independent of the gradiometer length: when the detector length is small compared to the wavelength of the seismic wave, both the GW and GGN signals appear as gradients; changing the length of the detector does not help to separate them. In the case of MIGA, the maximal length of the gradiometer will be 150 m and the Rayleigh wave speed of the medium surrounding the LSBB is $c_R \simeq 2.4$ km/s [31], which means that the approximation (20) is valid for $f \ll f_0 = \frac{c_R}{2\pi d_{ij}} = 2.5$ Hz. At higher detection frequencies, or for a longer detector, the complete expression in Eq. (19) must be used.

Figure 4 shows the equivalent strain induced by seismic GGN calculated from Eq. (18). For this projection we used data from the "RAS" seismic station, considering a depth of $h = 300$ m and using the propagation medium parameters that were previously measured at LSBB [32]: $\alpha \simeq 4.66$ km/s, $\beta \simeq 2.61$ km/s, and $\rho_0 = 2500$ kg/m³. To take into account the variability of seismic conditions shown in Fig. 2, the projections are done for the acceleration spectra corresponding to the 90th percentile of a noisy month and the 10th percentile of a quiet month.

We note that the strain limitation from seismic GGN is below the initial projected shot noise sensitivity of MIGA (light green curve) that comes from the use of standard AI techniques such as two-photon transitions and a 1 mrad/√Hz detection noise [22]. With an upgraded

version of the detector, using the large momentum transfer (LMT) of 2×100 photon transitions and an enhanced detection noise of 0.1 mrad/√Hz, we see in Fig. 4 that seismic GGN is barely detectable in the mHz range. Nevertheless, tests of GGN models with this improved detector—referred to in the following as iMIGA—will be possible considering long-term integration of the antenna data that will be described in Sec. V. The upgrade towards the iMIGA configuration should be possible on a time scale of a few years: it relies on LMT performances that were already demonstrated [33] and on an increase of atom flux to improve the detection noise by 1 order of magnitude with respect to the state of the art [34].

The seismic GGN model presented here relies on the assumption that the movement of the ground in the infrasound band can be described by a superposition of plane Rayleigh waves propagating in an isotropic and homogeneous medium. The importance of sea and ocean conditions on the local seismic activity, illustrated by the histograms in Fig. 2, reinforce the "Rayleigh dominating" hypothesis. However, previous studies [32] have shown a significant anisotropy in the karstic mountain range where MIGA will be operating and therefore other types of seismic waves could also contribute to the overall GGN. The measurements of the iMIGA configuration could help to improve such models.

IV. INFRASOUND GGN

We now consider the gravity gradient noise induced by adiabatic pressure variations propagating as sound waves in the atmosphere. We thus consider that relative density and pressure variations $\delta\rho/\rho_0$ and $\delta p/p_0$ within the atmosphere are linked by the adiabatic index γ,

$$\gamma \frac{\delta\rho(\vec{r}, t)}{\rho_0} = \frac{\delta p(\vec{r}, t)}{p_0}. \tag{21}$$

The gravity potential perturbation $\delta^3 U(\vec{r}_0, \vec{r}, t)$ at $\vec{r}_0$ induced by a single acoustic plane wave with wave vector $\vec{k}$ propagating in an infinitesimal volume $d^3\vec{r}$ centred at $\vec{r}$ is then

$$\delta^3 U(\vec{r}_0, \vec{r}, t) = -\frac{G\rho_0}{\gamma p_0} \delta p(\omega) \frac{e^{i(\vec{k}\cdot\vec{r} - \omega t)}}{|\vec{r} - \vec{r}_0|} d^3\vec{r}. \tag{22}$$

It must be noted that atmospheric density perturbations are not limited to the phenomena described by Eq. (21); we limit our study to "stationary" perturbations and discard transient perturbations induced by shock waves or airborne objects. Furthermore, given the average depth of the MIGA detector (about 300 m), gravity perturbations from atmospheric temperature fluctuations are believed to be much smaller [11,35]. Nevertheless a new formalism valid for the frequency window of interest here (10 mHz–1 Hz) would be needed to rule out this contribution definitively.
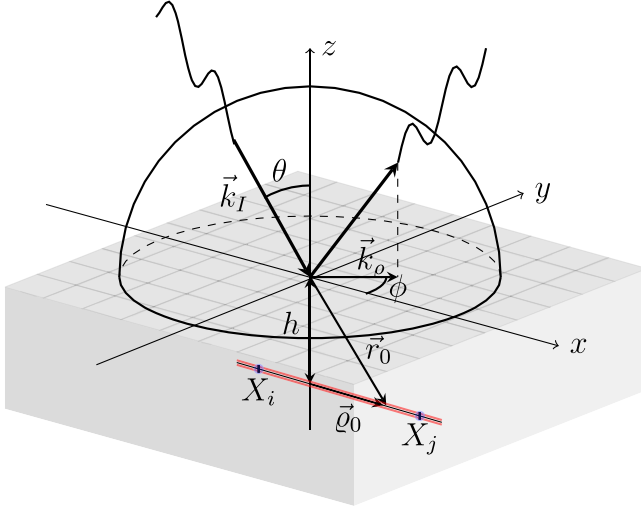
FIG. 5.   Sound wave modeling: angle and axis definition. $\vec{k}_I$ is the wave vector of the incident plane wave, with $\vec{k}_\varrho$ being its projection onto the horizontal plane, θ and ϕ are the incidence and azimuthal angle of the wave, h is the depth of the detector, $\vec{r}_0$ is the position where the gravity perturbation is calculated, with $\vec{\varrho}_0$ being its projection onto the horizontal plane, and X_i and X_j are the positions of the extremities of the gradiometer along the X axis.

We now consider that acoustic perturbations inside the atmosphere are described by an isotropic superposition of acoustic plane waves, and that each wave propagating along the direction (θ,ϕ) with wave vector $\vec{k}_I$ and velocity $v_s = 343$ m/s is totally reflected at the Earth's surface (see Fig. 5). To obtain the total gravity perturbation $\delta U(\vec{r}_0, t)$ induced at a point situated underground by such a wave, the contributions of the incident and reflected waves given by Eq. (22) must be integrated over the whole hemisphere. The result can be found in Ref. [11],

$$\delta U(\vec{r}_0, t) = -4\pi \frac{G\rho_0}{\gamma p_0} e^{i(\vec{k}_\varrho \cdot \vec{\varrho}_0 - \omega t)} \frac{\delta p(\omega)}{k_I^2} e^{-hk_I \sin\theta}, \quad (23)$$

where $\vec{\varrho}_0$ is the projection of $\vec{r}_0$ onto the horizontal plane. This gravity perturbation yields the acceleration:

$$\delta \vec{a}(\vec{r}_0, t) = -\frac{4\pi G\rho_0}{\gamma p_0} e^{i(\vec{k}_\varrho \cdot \vec{\varrho}_0 - \omega t)}$$
$$\times \frac{\delta p(\omega)}{k_I} e^{-hk_I \sin\theta} \sin\theta \begin{pmatrix} i\cos\phi \\ i\sin\phi \\ -1 \end{pmatrix}. \quad (24)$$

The acceleration created along the gradiometer direction at position $\vec{r}_0 = X\vec{e}_x - h\vec{e}_z$ is given by Eq. (25):

$$\delta a_x(X, t) = \kappa_I(k_I)\delta p(\omega) e^{-i\omega t} e^{ik_I X \sin\theta \cos\phi}$$
$$\times e^{-hk_I \sin\theta} \sin\theta i \cos\phi, \quad (25)$$

where $\kappa_I(k_I) = \frac{4\pi G\rho_0}{\gamma p_0 k_I}$. The spatial correlation function of the atmospheric GGN over the gradiometer can then be obtained from Eq. (10) by averaging over all of the different (θ, ϕ) directions ($\theta \in [0; \frac{\pi}{2}]$ and $\phi \in [0; 2\pi]$),

$$C^I(d_{ij}) = \kappa_I^2(k_I)S_{\delta p}(\omega)$$
$$\times \langle e^{ik_I d_{ij} \sin\theta \cos\phi} e^{-2hk_I \sin\theta} \sin^2\theta \cos^2\phi \rangle_{\theta,\phi}. \quad (26)$$

From Eq. (9), the infrasound GGN is then

$$S_{\Delta a_x}(d_{ij}, \omega) = \kappa_I^2(k_I)S_{\delta p}(\omega)\chi_1^I(k_I, d_{ij}), \quad (27)$$

where $\chi_1^I(k_I, d_{ij})$ gathers all correlation effects contributing to the GGN,

$$\chi_1^I(k_I, d_{ij}) = \langle 2(1 - \cos(k_I d_{ij} \sin\theta \cos\phi))$$
$$\times e^{-2hk_I \sin\theta} \sin^2\theta \cos^2\phi \rangle_{\theta,\phi}. \quad (28)$$

For $k_I d_{ij} \ll 1$ and $2hk_I \ll 1$, a low-frequency approximation can be obtained:

$$\chi_1^I(k_I, d_{ij}) \simeq \left(\frac{3}{8}\right)^2 k_I^2 d_{ij}^2. \quad (29)$$

For the parameters of MIGA, this approximation stands for $f = v_s/2\pi d_{ij} \ll 0.1$ Hz. In contradiction with the seismic case, this means that around its maximum sensitivity ($f \simeq 2$ Hz), the full expression Eq. (28) has to be used and the strain limitation induced by atmospheric GGN will depend on the distance between the test masses.

Using Eq. (27), we project the strain limitation induced by atmospheric GGN on future measurements by MIGA. To determine the local pressure spectrum, we conducted an on-site atmospheric pressure measurement campaign. We used an MB3 D microbarometer from Seismo Wave [36], able to resolve 1.75 mPa RMS in the 0.02–4 Hz window, with a self-noise at least 10 dB below Bowman's low-noise model [37]. The sensor was installed at about 500 m above the galleries of the LSBB and close to the future installation zone of MIGA inside the laboratory (see Fig. 6). The measurements were conducted during winter, covering a series of different weather conditions. To filter out wind-generated pressure noise [38] that can increase pressure variations by several orders of magnitude, we used a simple wind noise attenuator composed of a set of four tubes (1.5 m in length) pointing in the four directions. Figure 7 shows the amplitude spectral density of pressure variations as histograms for two 12-hour periods: a calm period with no wind and a noisier period associated with a light wind of about 5 m/s. A projection of the equivalent strain induced by infrasound GGN corresponding to these measurements is presented in Fig. 8. Under 0.02 Hz, the projection is performed using an extrapolation of the measurements using a pressure noise model derived from
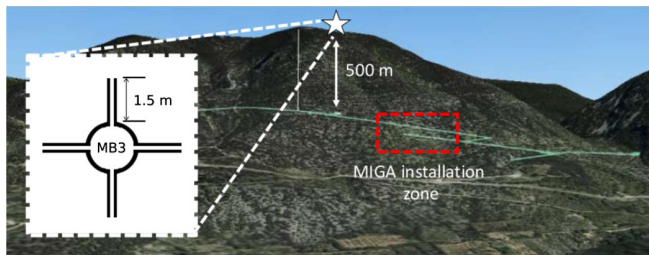
FIG. 6. Configuration of the pressure measurements at LSBB: an MB3 D microbarometer (white star) was installed on the surface about 500 m above the galleries of the LSBB (green lines) and close to the future installation zone of MIGA (red box). Inset: Schematic of the wind noise filter. The microbarometer (cylinder with a diameter of 11 cm) is placed at the center and the filtering pipes are 1.5 m long and 15 mm in diameter.
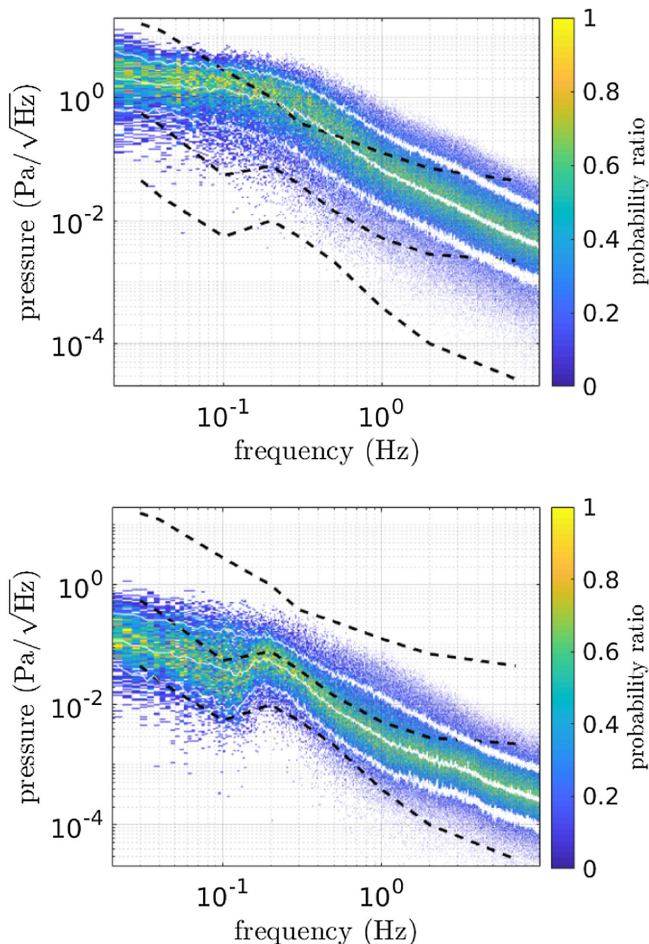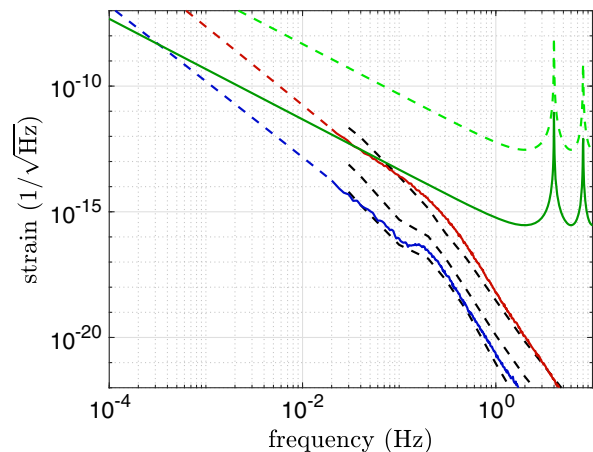

FIG. 8. MIGA strain sensitivity to infrasound GGN, with data taken from the Bowman model [37] (dashed black) and measured on site at LSBB (10th percentile of a calm period in blue, and 90th percentile of a windy period in red) with a low-frequency extrapolation such that $S(\delta p; \omega) = S_0 \omega^{-2.2}$ in accordance with low-frequency results reported in Ref. [39] (dashed blue and red lines). The detection noises for MIGA in its initial and improved configurations, calculated for $2T = 0.5$ s, are reported respectively in dashed and plain green lines.

the International Monitoring System stations [39]. We note that with the iMIGA configuration the infrasound GGN in noisy weather conditions starts to be detectable below 100 mHz.

Improvements upon MIGA could be used to develop more accurate infrasound GGN models that will be required for the future realization of low-frequency GW detectors. In this regard, we would like to draw the attention of the reader to the limitations of the current model presented here: the projection uses a pressure noise recorded with a single station which potentially includes a strong contribution that is noncoherent on the scale of a large detector, and thus cannot be modeled by plane waves. Such contributions would need to be estimated using multiple measurement stations in an antenna configuration like that of, for example, Matoza *et al.* [40]; it could then be accurately accounted for in the projection model.

V. TESTING GGN MODELS WITH MIGA

In the previous sections we have shown that enhanced versions of MIGA could enable GGN spectral analysis. However, due to SNR limitations, this method will be mainly limited to studies of atmospheric GGN, for frequencies under 100 mHz. A large fraction of the projected GGN power spectral density remains under the detection limit set by atom shot noise. Such background noise below the sensitivity threshold can contribute to measurable variations of the atomic phase after integration over an extended period of time. In this section, we present this data analysis method

FIG. 7. Histograms of the outside pressure variations 500 m above the future MIGA galleries for two weather conditions (an average wind velocity of 5 m/s average for the top plot, and no wind for the bottom plot), with the 10th, 50th, and 90th percentiles (white curves) and Bowman's low, middle, and high models (dashed black lines).

and calculate the Allan variance [41] of the averaged atomic phase from GGN.

With the notations introduced in Sec. II, the gradiometer configuration gives a differential interferometric phase,

$$\psi(X_i, X_j, t) = \Delta\phi_x(X_i, t) - \Delta\phi_x(X_j, t)$$
$$= n \int_{-\infty}^{+\infty} g'(\tau - t)(\Delta\varphi_{\text{las}}(X_i, \tau)$$
$$- \Delta\varphi_{\text{las}}(X_j, \tau))d\tau. \tag{30}$$

Considering that the gradiometer is operated sequentially with a cycling time T_c and that we average m consecutive measurements, we can obtain from Ref. [23] the Allan variance of the differential interferometric phase averaged over a time mT_c,

$$\sigma_\psi^2(mT_c) = \frac{n^2}{2m^2} \int_0^{+\infty} \frac{4\sin^4(m\omega T_c/2)}{\sin^2(\omega T_c/2)} |\omega G(\omega)|^2 S_\Gamma(\omega) \frac{d\omega}{2\pi}, \tag{31}$$

where $S_\Gamma(\omega)$ is the PSD of the differential laser phase noise $\Delta\varphi_{\text{las}}(X_i, \tau) - \Delta\varphi_{\text{las}}(X_j, \tau)$. Considering that this noise is coming from the acceleration of the atoms induced by GGN yields $S_\Gamma(\omega) = (\frac{2k_L}{\omega^2})^2 S_{\Delta a_x}(\omega)$, the Allan variance can be expressed as

$$\sigma_\psi^2(mT_c) = \int_0^{+\infty} H_m(\omega) S_{\Delta a_x}(\omega) \frac{d\omega}{2\pi}, \tag{32}$$

where H_m is the transfer function from GGN to the averaged differential atomic phase:

$$H_m(\omega) = \frac{8k_L^2 n^2}{m^2} \frac{\sin^4(m\omega T_c/2)}{\sin^2(\omega T_c/2)} \frac{|G(\omega)|^2}{\omega^2}. \tag{33}$$

Figure 9 shows the GGN power spectral density $S_{\Delta a_x}$ calculated for the largest gradiometer ($d_{ij} = 150$ m) available in MIGA. This PSD is obtained from the data and projection models presented in Secs. III and IV. We observe that under 100 mHz, the GGN grows rapidly as $f^{-2.2}$ and $f^{-4.6}$ for atmospheric and seismic contributions, respectively.

From Eq. (32) we then plot the Allan variance of the averaged atomic phase from GGN as a function of the integration time mT_c (see Fig. 10). Such calculations are done for the iMIGA configuration considering the contributions of atmospheric and seismic GGN and the detection limit set by atom shot noise. Remarkably, we observe that fluctuations of the atomic phase induced by atmospheric GGN in noisy weather conditions (purple curve) will be observable by averaging measurements over only a few seconds. Resolving fluctuations due to seismic activity would require averaging for longer periods, of the
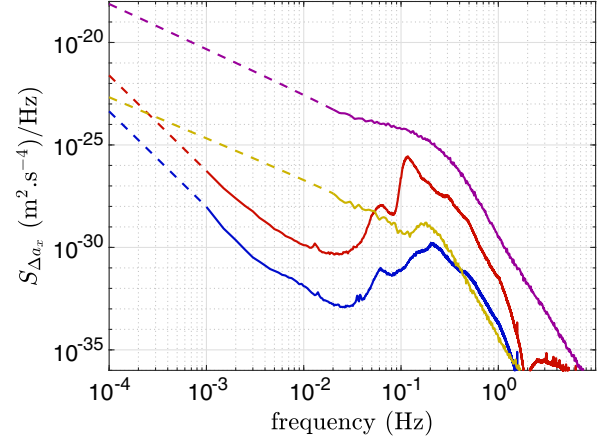

FIG. 9. Projections of the differential acceleration induced by GGN, calculated using infrasound and seismic data and their low-frequency extrapolations. The seismic 10th percentile during a quiet month (90th during a noisy month) is shown in blue (red), and the infrasound 10th percentile during a calm period (90th percentile during a windy period) is shown in yellow (purple).

order of a few tens of seconds; the long-term stability commonly achieved by cold atom experiments makes this entirely within reach. Looking at the low-frequency approximation ($\omega \ll 1/mT_c$) of the transfer function [Eq. (33)], that is,

$$H_m = 2k_L^2 n^2 m^2 T_c^2 T^4 \omega^2, \tag{34}$$

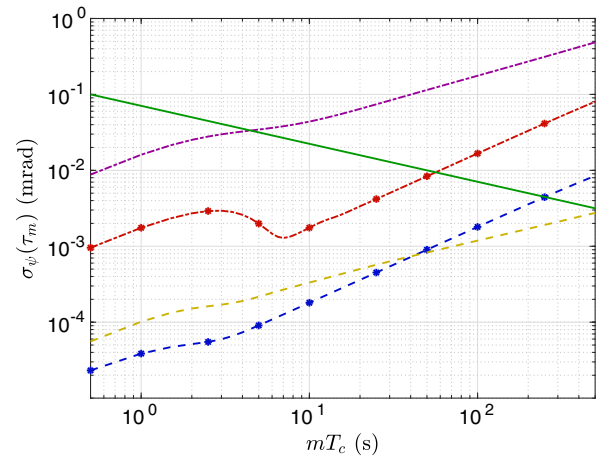FIG. 10. Allan standard deviation $\sigma_\psi(\tau_m)$ vs the measuring time mT_c. The cycle time is taken equal to the interrogation time: $2T = T_c = 0.5$ s. The calculation adopts the GGN acceleration spectra in Fig. 9: the seismic 10th percentile during a quiet month (90th during a noisy month) is shown as a dashed round-pointed blue line (dot-dashed round-pointed red line), and the infrasound 10th percentile during a calm period (90th percentile during a windy period) is shown as a dashed yellow line (dot-dashed purple line). The plain green line represents the detection noise for iMIGA.
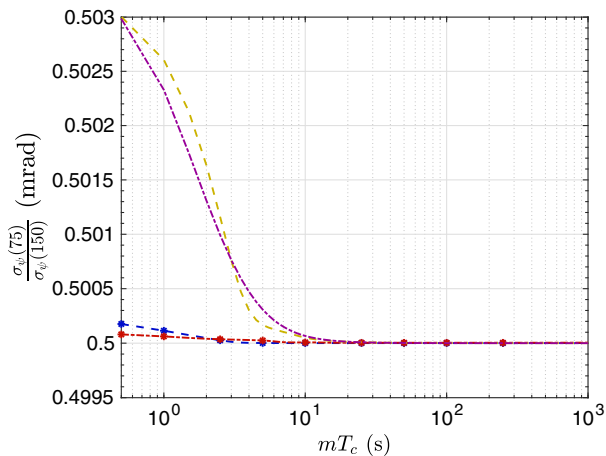
FIG. 11. Ratio of the Allan standard deviations of the averaged atomic phase for a data set that would be simultaneously acquired from the two gradiometers available in MIGA (baselines 150 and 75 m). The color coding and line types are the same as in Fig. 10.

we can get an intuitive understanding of why the Allan variance of the atomic phase from GGN grows rapidly as a function of the integration time: at low frequency, the weight of the low-frequency components of $S_{\Delta a_x}$ in the integral is proportional to m^2 and σ_ψ is dominated by those contributions as $S_{\Delta a_x}$ grows faster than ω^{-2}.

Integrating data would give access to GGN signals from atom gradiometry measurements. The Allan variance of the averaged atomic phase from GGN could be compared with the projected values obtained from simultaneous measurements of atmospheric pressure or local acceleration, which would allow to test the models presented in Secs. III and IV. Remarkably, comparing the Allan variance of the different gradiometric signals of MIGA could also validate some properties of the models without the need for extra seismic or atmospheric measurements. As the integration parameter m increases, the low-frequency components of $S_{\Delta a_x}$ become dominant in the sum of Eq. (32) and the approximations of Eqs. (20) and (29) become valid. This means that the averaged atomic phase σ_ψ of each gradiometer will tend to be proportional to its length. This effect was numerically tested (see Fig. 11) by calculating the ratio of the Allan standard deviations of the averaged atomic phase from GGN for the two gradiometers available in MIGA (with baselines of 150 and 75 m). After ten cycles, the ratio converges to the expected value of 0.5 by less than one per thousand.

VI. CONCLUSION

In this paper we have modeled the effect of the local gravitational field fluctuations on the MIGA underground AI and shown that the antenna will allow a study of these fluctuations. We projected the limitation of the strain sensitivity from seismic and atmospheric GGN using environmental data recorded at the LSBB low-noise laboratory, where MIGA is located. We have shown that the dominant contribution linked to ambient pressure variations outside the LSBB facility could become directly measurable for characteristic frequencies under 100 mHz. We also demonstrated that the integration of the antenna data on time scales of the order of a few tens of seconds could enable access to GGN signals with strong SNRs—data integration made possible thanks to the intrinsic long-term stability of cold atom experiments. This last method could refine current GGN models by comparing the measured Allan variance of the averaged atomic phase with its expected value from the projection of external seismic and pressure measurements, or by comparing the Allan variance of the different MIGA gradiometers. MIGA could provide relevant GGN characterization for state-of-the-art GW detectors, both in construction (KAGRA [42]) and planned (Einstein Telescope [43]), in relation to optimal site choice and measurement protocol for background GGN. It will constitute a study case for future sub-Hz GW detectors based on AI networks for the reduction of GGN [21].

[1] B. Abbott *et al.*, Phys. Rev. Lett. **116**, 061102 (2016).
[2] J. Aasi *et al.*, Classical Quantum Gravity **32**, 115012 (2015).
[3] B. Abbott *et al.* Phys. Rev. Lett. **116**, 221101 (2016).
[4] F. Acernese *et al.* Classical Quantum Gravity **32**, 024001 (2014).
[5] B. Abbott *et al.* Phys. Rev. Lett. **119**, 161101 (2017).
[6] B. P. Abbott *et al.* Astrophys. J. **848**, L12 (2017).
[7] D. Martynov *et al.* Phys. Rev. D **93**, 112004 (2016).
[8] I. Mandel, A. Sesana, and A. Vecchio, Classical Quantum Gravity **35**, 054004 (2018).
[9] A. Sesana, Phys. Rev. Lett. **116**, 231102 (2016).
[10] P. W. Graham and S. Jung, Phys. Rev. D **97**, 024052 (2018).
[11] J. Harms, Living Rev. Relativity **18**, 3 (2015).
[12] M. W. Coughlin, J. Harms, J. Driggers, D. J. McManus, N. Mukund, M. P. Ross, B. J. J. Slagmolen, and K. Venkateswara, Phys. Rev. Lett. **121**, 221104 (2018).
[13] O. Jennrich, Classical Quantum Gravity **26**, 153001 (2009).
[14] S. Sato *et al.*, J. Phys. Conf. Ser. **840**, 012010 (2017).
[15] M. A. Norcia, J. R. K. Cline, and J. K. Thompson, Phys. Rev. A **96**, 042118 (2017).
[16] N. Yu and M. Tinto, Gen. Relativ. Gravit. **43**, 1943 (2011).
[17] P. W. Graham, J. M. Hogan, M. A. Kasevich, and S. Rajendran, Phys. Rev. Lett. **110**, 171102 (2013).
[18] S. Kolkowitz, I. Pikovski, N. Langellier, M. Lukin, R. Walsworth, and J. Ye, Phys. Rev. D **94**, 124043 (2016).
[19] J. Harms, B. Slagmolen, R. Adhikari, M. Miller, M. Evans, Y. Chen, H. Müller, and M. Ando, Phys. Rev. D **88**, 122003 (2013).
[20] S. Dimopoulos, P. Graham, J. Hogan, M. Kasevich, and S. Rajendran, Phys. Rev. D **78**, 122002 (2008).
[21] W. Chaibi, R. Geiger, B. Canuel, A. Bertoldi, A. Landragin, and P. Bouyer, Phys. Rev. D **93**, 021101 (2016).
[22] B. Canuel *et al.*, Sci. Rep. **8**, 14064 (2018).
[23] P. Cheinet, B. Canuel, F. Pereira Dos Santos, A. Gauguet, F. Yver-Leduc, and A. Landragin, IEEE Trans. Instrum. Meas. **57**, 1141 (2008).
[24] P. Saulson, Phys. Rev. D **30**, 732 (1984).
[25] S. A. Hughes and K. S. Thorne, Phys. Rev. D **58**, 122002 (1998).
[26] D. Fiorucci, J. Harms, M. Barsuglia, I. Fiori, and F. Paoletti, Phys. Rev. D **97**, 062003 (2018).
[27] S. Gaffet, J. Wang, M. Yedlin, G. Nolet, C. Maron, D. Brunel, A. Cavaillou, D. Boyer, C. Sudre, and M. Auguste, IRIS Data Serv. Newsl. **11**, 3 (2009).
[28] J. R. Peterson, Observations and modeling of seismic background noise, Open-File Report No. 93-332. U.S. Department of Interior, Geological Survey, Albuquerque, New Mexico, 1993, p. 94, https://doi.org/10.3133/ofr93322.
[29] F. Ardhuin, L. Gualtieri, and E. Stutzmann, Geophys. Res. Lett. **42**, 765 (2015).
[30] S. Stein and M. Wysession, *An Introduction to Seismology, Earthquakes and Earth Structure* (Wiley-Blackwell, Hoboken, New Jersey, 2003), p. 512, ISBN 978-1-118-68745-1.
[31] The speed of the Rayleigh waves c_R was computed [30] from the speed of the secondary waves $\beta \simeq 2.61$ km/s [32] such that $c_R = 0.92\beta$.
[32] J. Bereš, H. Zeyen, G. Sénéchal, D. Rousset, and S. Gaffet, J. Appl. Geophys. **94**, 59 (2013).
[33] S. w. Chiow, T. Kovachy, H. C. Chien, and M. A. Kasevich, Phys. Rev. Lett. **107**, 130403 (2011).
[34] A. Gauguet, B. Canuel, T. Lévéque, W. Chaibi, and A. Landragin, Phys. Rev. A **80**, 063604 (2009).
[35] T. Creighton, Classical Quantum Gravity **25**, 125011 (2008).
[36] http://www.seismowave.com.
[37] J. R. Bowman, G. E. Baker, and M. Bahavar, Geophys. Res. Lett. **32**, L09803 (2005).
[38] B. Alcoverro and A. Le Pichon, J. Acoust. Soc. Am. **117**, 1717 (2005).
[39] J. Marty, D. Ponceau, and F. Dalaudier, Geophys. Res. Lett. **37**, L19802 (2010).
[40] R. S. Matoza, M. Landès, A. Le Pichon, L. Ceranna, and D. Brown, Geophys. Res. Lett. **40**, 429 (2013).
[41] D. Allan, Proc. IEEE **54**, 221 (1966).
[42] Y. Aso, Y. Michimura, K. Somiya, M. Ando, O. Miyakawa, T. Sekiguchi, D. Tatsumi, and H. Yamamoto, Phys. Rev. D **88**, 043007 (2013).
[43] M. Punturo *et al.*, Classical Quantum Gravity **27**, 194002 (2010).